



Full length article

The synergic role of collagen and citrate in stabilizing amorphous calcium phosphate precursors with platy morphology



José Manuel Delgado-López^{a,b,*}, Federica Bertolotti^a, Jeppe Lyngsø^c, Jan Skov Pedersen^c, Antonio Cervellino^d, Norberto Masciocchi^a, Antonietta Guagliardi^{e,*}

^a Dipartimento di Scienza e Alta Tecnologia and To.Sca.Lab, Università dell'Insubria, Como, Italy

^b Instituto Andaluz de Ciencias de la Tierra (IACT, CSIC-UGR), Armilla (Granada), Spain

^c Interdisciplinary Nanoscience Center (iNANO) and Department of Chemistry, Aarhus University, Aarhus C, Denmark

^d Swiss Light Source, Paul Scherrer Institut, Villigen, Switzerland

^e Istituto di Cristallografia and To.Sca.Lab, CNR, Como, Italy

ARTICLE INFO

Article history:

Received 13 August 2016

Received in revised form 19 October 2016

Accepted 17 November 2016

Available online 18 November 2016

Keywords:

Bone mineralization

SAXS/WAXS

Citrate

ACP

AFM

Collagen

Nanoparticle

Biomaterials

ABSTRACT

Bioinspired *in vitro* collagen mineralization experiments have been performed in the presence of citrate and the combined role of the two bone organic matrix components in controlling mineral formation was investigated for the first time. Mineralized and non-mineralized collagen fibrils have been in depth characterized by combining small- and wide-angle X-ray scattering (SAXS/WAXS) techniques with Atomic Force Microscopy (AFM) imaging. A synergic effect of collagen and citrate in driving the formation of long-term stable amorphous calcium phosphate (ACP) nanoparticles with platy morphology was found. AFM images on mineralized collagen fibrils revealed that some of the ACP nanoparticles were deposited on the intramolecular nanoscopic holes of collagen fibrils.

Statement of Significance

Citrate is an important component of the bone organic matrix but its specific role in bone mineralization is presently unclear. In this work, bioinspired *in vitro* collagen mineralization experiments in the presence of citrate have been carried out and the combined role of collagen and citrate in controlling mineral formation has been addressed for the first time. Through X-ray scattering and Atomic Force Microscopy characterizations on mineralized and non-mineralized collagen fibrils, we have found that citrate in synergy with collagen stabilizes an amorphous calcium phosphate (ACP) phase with platy morphology over one week and controls its deposition on collagen fibrils.

© 2016 Acta Materialia Inc. Published by Elsevier Ltd. All rights reserved.

1. Introduction

Bone is a composite material with an extremely complex structure exhibiting many levels of organization [1–6]. Mineralized collagen fibrils are the building blocks of such a complex architecture. Collagen triple-helix molecules self-assemble in a periodic axially staggered array forming the so-called fibrils (100–300 nm in diameter), which exhibit a characteristic banding pattern of 67 nm, where a densely packed 27 nm-long region (the so-called overlap zone) alternates with the less dense 40 nm-long gap zone [1,5,7,8]. This organic matrix is further reinforced by an array of

plate-shaped apatite nanocrystals, both through intra- (within the fibrils) and inter- or extra-fibrillar (on the fibrils surface) mineralization. In the intrafibrillar mineralization, the platelets pile up [3] on their largest {01–10} hexagonal facets and elongate with their crystallographic *c*-axis parallel to the collagen fibrils axis, resulting in an organic/inorganic composite with unique biomechanical properties. Gaining a better understanding of the mechanisms of this biologically controlled mineral formation at the molecular level is of paramount importance to design new therapeutic engineered scaffolds for repairing or regenerating hard tissues [2,9].

Thanks to the intensive investigation on biological samples complemented by *in vivo* and *in vitro* studies, great advances have been reached over the years on the role of the organic matrix (*i.e.* collagen fibrils, non-collagenous proteins (NCPs) and small molecules), exerting a high level of control over the composition,

* Corresponding authors at: Dipartimento di Scienza e Alta Tecnologia and To.Sca.Lab, Università dell'Insubria, Como, Italy (J.M. Delgado-López) and Istituto di Cristallografia and To.Sca.Lab, CNR, Como, Italy (A. Guagliardi).

E-mail addresses: jmdl@iact.ugr-csic.es (J.M. Delgado-López), antonella.guagliardi@ic.cnr.it (A. Guagliardi).

structure, size and morphology and organization of the mineral phase [1,4,5,7,10–15]. However, an overall exhaustive comprehension of the mechanism is still to be attained and many issues either on the specific action or the interplay between the different organic players, and on the mineral component as well, need to be elucidated [7,12,14].

Two different mineralization pathways are nowadays explored through *in vitro* experiments. In line with the mechanism relying on classical nucleation, Nassif and co-workers [12] were able to mineralize collagen fibrils *in vitro* in the absence of any organic/polymeric additives, with side chains of polypeptide charged amino acids of collagen likely providing the binding sites for calcium and phosphate ions of the (supersaturated) mineralizing solution [16]. On the other hand, many *in vitro* experiments carried out in the presence of either selected NCPs or polypeptides rich in poly-carboxylic acids (e.g., poly-aspartic acid), mimicking the poly-anionic character of the NCPs [1,7,10,11,13,14], demonstrated their role in controlling the mineral nucleation and growth. The rationale behind such an approach is that mineral deposition occurs *via* a non-classical nucleation mechanism, involving the precipitation of an amorphous precursor, which infiltrates into the nanoscopic gaps of the assembled collagen fibrils and further transforms into platy nanocrystalline apatite [1,13,14,17,18]. Nano-spheres of amorphous calcium phosphate (ACP) have been observed at the early stages of mineralization [19,20], whereas thin apatite platelets are observed at the final crystalline phase. However, the mechanism underlying the origin of this platy morphology still remains unclear [4]. Making this situation even more complex, recent solid-state NMR studies have shown that citrate, a small molecule of the organic bone components somewhat neglected so far, occurring in a relatively large amount (~5.5 wt %, which accounts for ~80% of all citrate in the body [21]), is strongly bound to bone apatite and controls the platelet thickness [22]. This finding opened new scenarios in bone mineralization, where citrate might play a broader role than has been thought to date [23]. Inspired by this study, in a previous work [24] we have investigated the role of citrate in a simplified system model (without collagen) providing experimental evidence of its role in controlling the size and morphology of apatite nanoparticles (NPs) likely inherited from an amorphous precursor of platy morphology.

In this work we focus on *in vitro* collagen mineralization experiments, aimed at gaining a better understanding of the role of citrate in bone mineral formation. Here, we address particular attention to the nature and morphology of the first formed mineral phase when both collagen and citrate are at work. To this aim, collagen fibrils were mineralized in the presence of citrate under physiological conditions ($T = 37\text{ }^{\circ}\text{C}$ and $\text{pH} = 7.4$) and in-depth characterized through a combination of X-ray scattering (both in the small (SAXS) and the wide angle (WAXS) regions) and imaging (Atomic Force Microscopy, AFM) techniques. Wide-angle synchrotron X-ray scattering enabled us to measure simultaneously the scattering originating from the mineral precipitated at the early stages and from the collagen molecular arrangement within the fibrils (the so-called equatorial lateral packing). The morphology of the mineral phase was investigated by SAXS and AFM, the latter providing also the direct observation of both mineral deposition on collagen fibrils and mineral precipitation outside the fibrils and trapped within the composite.

2. Materials and methods

2.1. Reagents and solutions

2.1.1. Collagen stock solutions

Type I collagen gel, extracted from equine tendon using the standardized manufacturing method of Opocrin S.p.A. (Corlo di

Formigine, Modena, Italy) as described elsewhere [25], was kindly provided by Dr. Michele Iafisco (Institute of Science and Technology for Ceramics, ISTEC-CNR, Italy). Then, 1 g of type I collagen gel was diluted in 10 mL of acetic acid (0.1 M) and stirred overnight. The collagen solution was centrifuged at 5000 rpm for 15 min and the supernatant was collected and stored at $4\text{ }^{\circ}\text{C}$. The pH of the supernatant was 2.7. The concentration of collagen in this stock solution was 0.5 mg mL^{-1} , as measured by UV spectroscopy.

2.1.2. Mineralizing solutions

High purity $\text{CaCl}_2 \cdot 2\text{H}_2\text{O}$, Na_2HPO_4 , K_2HPO_4 , $\text{Na}_3\text{Cit} \cdot 2\text{H}_2\text{O}$ (where Cit is $\text{C}_6\text{H}_5\text{O}_3^{3-}$) and Hepes (4- [2-hydroxyethyl]-1-piperazineethane sulfonic acid) buffer were purchased from Sigma-Aldrich. All the solutions were prepared using ultrapure MilliQ water ($\rho = 18.2\text{ M}\Omega\text{ cm}$ at $25\text{ }^{\circ}\text{C}$).

2.1.3. Mineralization experiments

The collagen-containing solution ($\text{pH} 2.7$, 0.5 mg mL^{-1}) was mixed to a Ca- and citrate-containing solution. Then, a phosphate-containing solution was added to the latter mixture. All the solutions were prepared in Hepes buffer (10 mM, $\text{pH} 7.4$). Taking inspiration, from our previous work on citrate-controlled apatite nanoparticles [24] on one hand, and from the study on collagen mineralization in the presence of poly-aspartic acid (p-Asp) by Nudelman et al. [7], on the other hand, two series of experiments were performed, employing two different Ca: Cit ratios (1:4 and 1:2, respectively). The following concentrations were used: (1) 5.0 mM CaCl_2 , 20.0 mM sodium citrate and 6.0 mM NaH_2PO_4 (as in Ref. [24]); these samples are referred to as MinCol_1_4; (2) 2.7 mM CaCl_2 , 5.4 mM sodium citrate and 1.35 mM NaH_2PO_4 (as in Ref. [7], but with citrate replacing pAsp); these samples are referred to as MinCol_1_2. The mixtures were then matured at $37\text{ }^{\circ}\text{C}$ for 5 min, 96 h or 168 h in a thermostated oven. A blank Ref. sample containing only collagen in Hepes ($\text{pH} 7.4$, referred to as Col) was also prepared. Using the same concentrations as in (1), parallel blank mineralization experiments, either without citrate (MinCol_1_0) or without collagen (Min_1_4), were also prepared (maturation times: 24 h). Table 1 summarizes the concentrations used in the mineralization experiments. After maturation, the samples were repeatedly washed with MilliQ water by centrifugation (9000 rpm, 10 min, Centrifuge 5810 R, Eppendorf.) and the wet precipitates were freeze-dried overnight at $-50\text{ }^{\circ}\text{C}$ (LyoQuest, Telstar). Then, they were stored at room temperature until further characterization.

2.1.4. Synchrotron X-ray total scattering measurements

Dry samples were loaded in glass capillaries of 1.0 mm diameter and measured at the X04SA-MS Beamline of the Swiss Light Source (SLS) of the Paul Scherrer Institut (PSI, Villigen, Switzerland). The beam energy was set at 16 keV and the operational wavelength ($\lambda = 0.77449\text{ \AA}$) precisely determined by collecting, under the same experimental conditions, a silicon powder standard [NIST 640c, $a_0 = 0.54311946(92)\text{ nm}$ at $22.5\text{ }^{\circ}\text{C}$]. Data were collected in the $2\text{--}120^{\circ} 2\theta$ range with the aid of the position sensitive single-photon counting MYTHEN II detector [26]. Independent He/air and capillary scattering curves, as well as sample-loaded capillary transmission coefficients, were also measured and used for data subtraction of all extra-sample scattering effects and absorption corrections [27]. The linear absorption coefficient for the empty capillary was calculated on the basis of glass composition. Additionally, an X-ray powder diffraction pattern of the Min_1_4 sample was recorded using a Rigaku Miniflex 300 diffractometer with Bragg-Brentano geometry in the $\theta:2\theta$ mode (Ni-filtered $\text{Cu K}_{\alpha 1,2}$ radiation, $\lambda = 1.5418\text{ \AA}$).

Table 1
Summary of the concentrations (and corresponding acronyms) used in the mineralization experiments.

Acronym	[Collagen] (mg mL ⁻¹)	[CaCl ₂] (mM)	[Na ₃ Cit] (mM)	[Na ₂ HPO ₄] (mM)	pH
Col	0.2	0	0	0	7.4
MinCol_1_4	0.2	5	20	6	7.4
MinCol_1_2	0.2	2.7	5.4	1.35	7.4
MinCol_1_0	0.2	5	0	6	7.4
Min_1_4	0	5	20	6	7.4

2.1.5. The atomic pair distribution function

The atomic Pair Distribution Function (PDF) in the form of reduced $G(r)$, providing a histogram of the interatomic distances within the sample [28], was used here in order to obtain atomistic details on the ACP component of the mineralized collagen (MinCol_1_2) with 5 min of maturation time. In order to extract the PDF of the ACP component we calculated the differential PDF (d-PDF), by performing the difference between the total X-ray powder diffraction pattern and the one of the pure collagen. This subtraction was made in reciprocal space rather than in real space in order to limit the propagation of systematic truncation errors in the resulting d-PDF. For the sake of comparison, the atomic PDF of a citrate-controlled ACP sample precipitated in the absence of collagen was also analysed.

The total scattering function $S(Q)$ was obtained from the above mentioned X-ray powder diffraction patterns using the PDFgetX3 program [29]. The sine-Fourier transform was then applied to the reduced total scattering structure function, $F(Q) = Q[S(Q) - 1]$, obtaining the $G(r)$ function:

$$G(r) = \frac{2}{\pi} \int_{Q_{min}}^{Q_{max}} Q[S(Q) - 1] \sin Qr \, dQ$$

where $Q = 4\pi \sin \theta / \lambda$ is the magnitude of the scattering vector, $Q_{min} = 15 \text{ nm}^{-1}$ in order to avoid the small angle signals and $Q_{max} = 120 \text{ nm}^{-1}$, determined by the maximum angular resolution of the experimental data.

2.1.6. SAXS

The SAXS measurements were performed at the flux-optimized SAXS instrument (Bruker AXS) [30] located at the Interdisciplinary Nanoscience Center (iNANO), Aarhus University (Aarhus, Denmark). The instrument uses a Ga metal jet X-ray source and homebuilt scatterless slits [31]. The dry samples in glass capillaries of 1.0 mm diameter were mounted vertically in the integrated vacuum of the instrument. The beam cross section was broader ($\sim 1.5 \text{ mm}$) than the capillaries, however the SAXS patterns showed no discernible reflections from the capillary. As a first step, the scattering from an empty capillary was subtracted as background. In order to have the scattering from the inorganic nanoparticles, the scattering from pure collagen was subtracted from the other samples.

The SAXS data were analysed by fitting models to the data by means of least-squares methods [32]. The low Q -part of the SAXS data could be fitted by a model with monodisperse triaxial ellipsoids; however, in order to fit the high- Q part well, an additional contribution had to be included: respectively, a model for polydisperse spherical particle, a bimodal Gaussian distribution of spheres and an ellipsoid of revolution were tested for this contribution. The width of the distributions of the spheres could not be fitted independently since it provided too many fit parameters, accordingly they were fixed at σ values of 4 and 2 Å. Comparable best fits were obtained for both a bimodal population of spheres and the ellipsoidal contribution, and it is the results for these models that are reported.

The relative volume fraction and number density of particles in the two contributions were calculated from the forward scattering $I(0)_i$ values of the two contributions, as follows:

$$I(0) = I(0)_1 + I(0)_2 = k(n_1 V_1^2 \Delta \rho_1^2 + n_2 V_2^2 \Delta \rho_2^2)$$

where the indices refers to either the bimodal population of spheres or the ellipsoid of revolution (1) and the triaxial ellipsoid (2). The parameter n_i is the particles number density, V_i is the particle volume and $\Delta \rho_i$ is the scattering length density contrast of the particle and k is a scale factor. We assume that the contrast of the two types of particles is the same. Accordingly, $n_i = I(0)_i / k \Delta \rho^2 V_i^2$ and, the relative number density of particles $n_1/n_2 = I(0)_1 V_2^2 / I(0)_2 V_1^2$. Similarly, as the volume fraction of the i -th component is $\eta_i = n_i V_i$, the relative volume fractions of the two types of particles is $\eta_1/\eta_2 = I(0)_1 V_2 / I(0)_2 V_1$.

2.1.7. Atomic Force Microscopy observations

AFM was used for imaging dry mineralized (MinCol_1_2) and non-mineralized (Col) collagen fibrils. This high-resolution imaging technique is particularly suitable for measuring the thickness of nanoparticles with sub-nanometer resolution [33]. After washing, a drop of the slurry containing collagen fibrils was deposited on the atomically flat surface of a freshly cleaved mica substrate. After 1 min, the mica surface was repeatedly washed with MilliQ water and dried overnight at room temperature. Both non-mineralized and mineralized collagen fibrils were imaged with a NT-MDT scanning probe microscope (model BL022) by scanning the surface in semi-contact mode with silicon probes NGS01 (5.1 N m⁻¹ and 150 kHz, NT-MDT).

3. Results

The WAXS pattern of non-mineralized collagen in the Q region 2.5–50 nm⁻¹ (Col in Fig. 1a) provides structural information of collagen molecular arrangements. The peak at $Q = 5.43 \text{ nm}^{-1}$ gives information on the lateral packing of the triple-helix collagen molecules resulting, in our sample, in a d -spacing of 1.16 nm¹. This value is in excellent agreement with those reported for non-mineralized collagen from biological tissues, in dry conditions [34–36]. Additionally, other features arising from the diffuse scattering of collagen ($Q = 15.20 \text{ nm}^{-1}$) and from the axial periodicity of polypeptide subunits (helical rise, $Q = 21.74 \text{ nm}^{-1}$) are clearly visible [36]. Fig. 1a also shows the WAXS patterns collected on MinCol_1_4 samples at increasing maturation times. These patterns are very similar to that of pure collagen, irrespective of the maturation time, indicating that, at the relatively high Cit to Ca ratio used in these mineralization conditions, neither the intrafibrillar mineralization nor even the formation of any mineral phase(s) was detected. However, the instantaneous precipitation of nanocrystalline apatite (Ap) was detected with the same mineralizing solution, both in the

¹ Strictly speaking, following the assumption of a pseudo-hexagonal packing [8], the observed d -spacing, corresponding to the 100 reflection, must be transformed into an average intermolecular distance of ca. 1.34 nm by the (often disregarded) $2/\sqrt{3}$ factor, thus providing a more accurate quantitative estimate of the geometrical assembly in the equatorial plane.

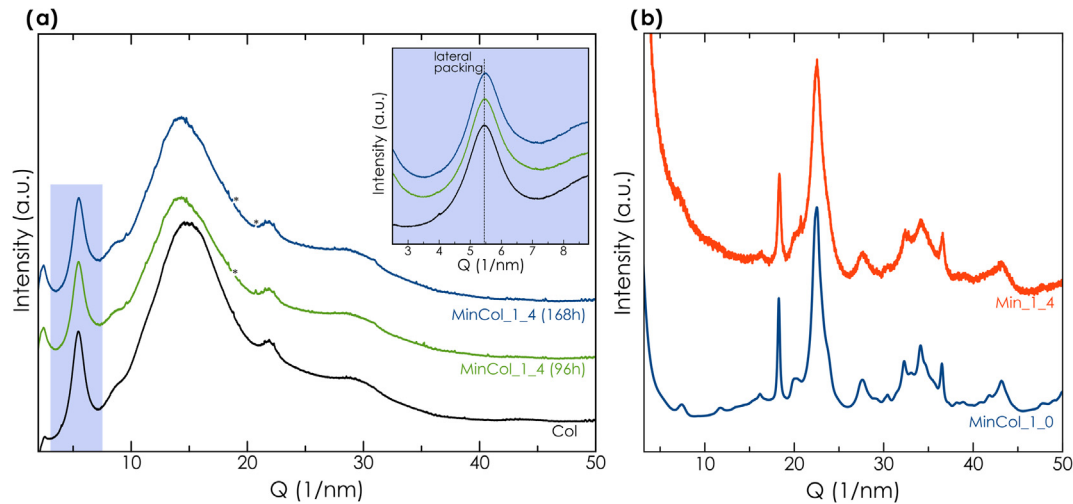


Fig. 1. a) WAXS patterns of pure collagen (Col) and MinCol_1_4 samples, the latter at increasing maturation time. The asterisks indicate the location of sharp peaks due to contaminating salts (NaCl and/or KCl) precipitated during drying process, which have been removed for the sake of clarity. The inset shows a magnification of the low-angle region highlighting the diffraction peak originating from the lateral packing of collagen. b) WAXS patterns of nanocrystalline apatite obtained either in the presence of *only* collagen (MinCol_1_0) or *only* citrate (Min_1_4).

presence of *only* collagen (MinCol_1_0, Fig. 1b) and in the presence of *only* citrate (Min_1_4, Fig. 1b). According to these findings, the lack of any (amorphous or crystalline) mineral phase in MinCol_1_4 samples, suggests a synergistic control on the mineral precipitation when collagen and citrate are together at work, at physiological pH and temperature.

Fig. 2a shows the WAXS patterns collected on mineralized collagen MinCol_1_2 samples at increasing maturation times. The fingerprinting properties of WAXS makes it a unique tool for recognizing the amorphous or crystalline nature of the phase(s) precipitated at the earliest stages of the mineralization, and for monitoring its continuous growth upon maturation. As long as the amount of mineral is small, the trace of the weakly scattering collagen matrix is also discernible, as in Fig. 2a. Here, beside collagen-related features, new broad peaks centred at $Q \sim 4.08 \text{ nm}^{-1}$ (low-angle region, inset in Fig. 2a) and

$Q \sim 21.36 \text{ nm}^{-1}$ (wide-angle region, Fig. 2a) emerge due to the precipitation of ACP [24]. The intensity of both peaks increases upon maturation, indicating a slightly larger amount of mineral (varying from ca. 6.4 to 9.5% in weight, as estimated by considering the areas of collagen and ACP signals under the WAXS curves and after normalization to electron units). However, the precipitation of the mineral phase is not affecting the position of the sharp(er) low angle collagen peak, which remains unchanged upon maturation (inset in Fig. 2a), as resulting from the peak fitting analysis (Fig. S1, Supplementary data). This finding suggests that the lateral arrangement of collagen molecules (which may be influenced by the intra-fibrillar mineralization) is not “perturbed” by the precipitation of the amorphous precursor detected in these experiments.

The analysis of the ACP contained in the MinCol_1_2 at 5 min was further complemented with the differential pair distribution function (d-PDF, Fig. 2b). The first two peaks are assigned to the

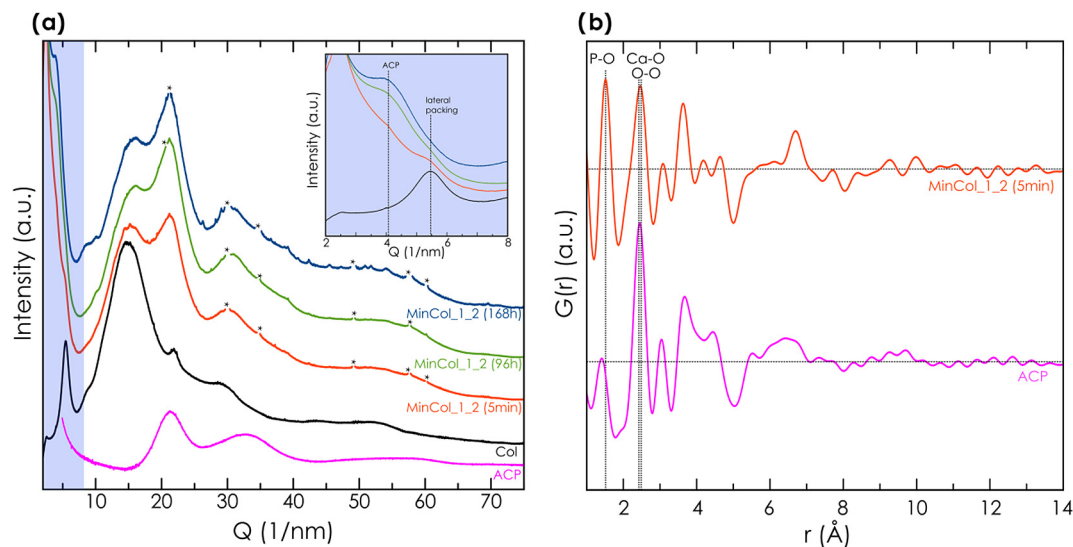


Fig. 2. a) WAXS patterns of collagen non-mineralized (Col) and mineralized (MinCol_1_2) samples, the latter at increasing maturation time. The asterisks and the inset have the same meaning as in Fig. 1. For comparison the pattern of ACP precipitated in the absence of collagen is also shown. The inset shows a magnification of the low-angle region highlighting the peaks related to the collagen lateral packing and the ACP component. b) d-PDF curve, in the form of the reduced $G(r)$, providing a plot of atomic number density vs atomic separations obtained for the ACP precipitated in the presence of collagen (MinCol_1_2, 5 min). For comparison, the PDF of ACP obtained in the absence of collagen is shown. The dotted vertical lines indicate the P-O (1.5 Å), Ca-O (2.4 Å) and O-O (2.5 Å) interatomic distances.

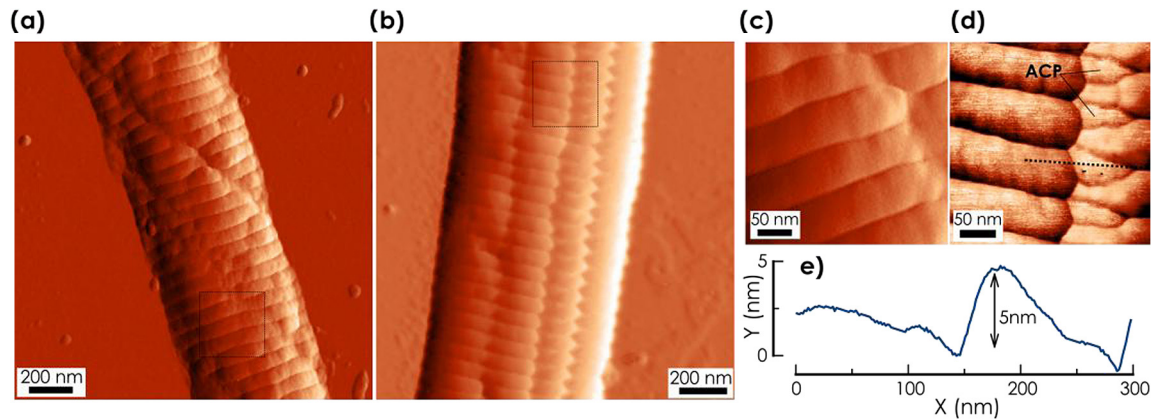


Fig. 3. AFM images of non-mineralized (a,c) and mineralized (maturation time: 168 h) (b,d) collagen fibrils. High-resolution AFM images in c and d were collected from the dotted squares in a and b, respectively. The vertical section in (e), which corresponds to the dotted line in d, reveals the platy morphology of deposited ACP particles.

nearest-neighbour P-O (1.5 Å), Ca-O (2.4 Å) and O-O (2.5 Å) interatomic distances, respectively. For comparison, the PDF curve from a sample containing pure ACP is shown in Fig. 2b, which shows Ca-O and O-O peaks at the same position as in the previous case, whereas the P-O distance appears slightly contracted (1.4 Å), likely due to the presence of some amount of CO_3^{2-} replacing PO_4^{3-} anions (the synthesis, which included sodium carbonate, is described in detail in Ref. [24]). Indeed, considering the lower coordination number of C in the CO_3^{2-} group compared to that of P in PO_4^{3-} and the reduced C-O distance (C-O \approx 1.3 Å vs P-O \approx 1.5 Å), the shift towards lower r values and the different area under the peak in the pure ACP sample is likely to result from the contribution of both C-O and P-O distances. The two components are indistinguishable in the $G(r)$ shown in Fig. 2b, owing to the real space resolution in our experiment $\Delta r = \pi/Q_{\text{max}} = 0.26$ Å (see Ref. [37]). Noticeably, the PDF function suggests that the ACP maximum correlation length in both cases does not extend over 10 Å. This value is in agreement with the radius of the apatite building unit, the so-called Posner's cluster [38] as well as the size of stable pre-nucleation clusters forming in simulated body fluids (SBF), proposed as precursors in ACP nucleation [39,40].

Non-mineralized and mineralized collagen fibrils were investigated by combining AFM and SAXS. For the MinCol_1_2 series further details were obtained both on the location, morphology and size of the ACP particles detected by WAXS. AFM images depicted in Fig. 3a–b show collagen fibrils with diameters ranging between 100 and 500 nm. The typical 67-nm patterning was clearly observed in both non-mineralized and mineralized samples (Fig. 3a and b, respectively). The high-resolution AFM images of mineralized fibrils show the precipitation of ACP both on the surface of (Fig. 3d) and outside the collagen fibrils (Fig. S2), both exhibiting platy morphology. Despite being rather unusual, this morphology has been already reported for ACP NPs, either driven by citrate [24,41] (later evolving into nanocrystalline apatite platelets) or precipitating in the absence of citrate as an intermediate floccular-like phase transforming into microcrystalline OCP [42]. Fig. 3d also reveals that the elongated aggregates (length: 60–80 nm; width: 30–40 nm; thickness: 4–6 nm range, Fig. 3e) are deposited on the nanoscopic holes (6–9 nm, the so-called *a-band* of the gaps [7]) which correspond to the intramolecular spaces between N- and C-terminal ends of collagen molecules [7]. These ACP NPs are not randomly deposited but follow the repeating 67-nm pattern of collagen fibrils. Fig. 3c shows the same *a-band* free of mineral in the non-mineralized collagen fibrils.

Fig. 4 shows the SAXS signals of the MinCol_1_2 and Col samples. Signals from non-mineralized collagen exhibit a Q^{-4} like scat-

tering in most of the Q -range, whereas the data from mineralized collagen show a different dependence due to the presence of the inorganic nanoparticles along with the organic matrix. These particles were firstly modelled by a triaxial ellipsoid form factor describing a single population of platy-shaped nanoparticles (as suggested by AFM, Fig. 3d,e), which correctly fits the experimental data at low Q , but leaves the high Q data unexplained. Adding a polydisperse sphere form factor resulted in a poor agreement, whereas a good fit in the whole Q range was obtained by using an additional ellipsoid form factor, suggesting the occurrence of smaller nanoparticles, still of platy morphology, with sizes of ca. 4 nm \times 1.2 nm at 5 min, and slight modifications at longer maturation time (Table 2). However, comparable results were also obtained with an alternative model for the high- Q region, which included a bimodal population of spheres, the largest sizes being in the 4.6–5.6 nm range and the smallest ones in the 2.6–3.2 nm range (Table 2). The two competing models confirm that the solution may not be unique and it might be possible to find other models that can fit the data equally well.

This description in terms of two populations suggests that two families of ACP nanoparticles, one of larger and one of smaller nanoparticles, are formed during the precipitation of the amorphous precursors. The sizes of the larger population (Table 2) are nearly constant upon maturation, being ca. 50–60 nm long, 30–40 nm wide and 6–8 nm thick, and match the sizes observed in AFM images. The relative volume fraction (η_1/η_2) indicates that the number of particles of smaller sizes decreases upon maturation (Table 2). SAXS data collected on the MinCol_1_4 samples are very similar to that of non-mineralized collagen and therefore are not shown here for the sake of clarity.

4. Discussion

On the basis of the experimental evidence presented in Figs. 1–4, we firstly outline the citrate concentration dependence of the ACP precipitation, in line with the citrate Ca-complexing action, but which is now further modulated by the presence of collagen. The citrate/ Ca^{2+} ratio of 4 inhibits the precipitation of any mineral phase (Fig. 1), which is known to be nearly instantaneous for the same conditions in the absence of collagen (Fig. 1b and Ref. [24]). However, by reducing the citrate/ Ca^{2+} ratio to 2, the precipitation of ACP was undoubtedly detected by WAXS. ACP was also found as the *unique* mineral species after one week of maturation at 37 °C. This finding suggests that, in the presence of collagen, the transformation of ACP into a more stable crystalline phase is inhibited by citrate ions likely adsorbed on the steadily growing

amorphous particles. This is clearly different from what was observed in previous *in vitro* mineralization experiments without collagen [24,43,44]. In contrast to our previous experiments without collagen [24], in which we accurately quantified the amount of citrate in the precipitated nanopowders and estimated a citrate coverage on apatite NPs very close to than found in biological samples [22], in the present study the co-presence of citrate and collagen fibrils makes a precise quantification of citrate in the composite highly difficult. That a different adsorption is taking place (though not quantitatively determined) at the different ini-

tial citrate concentration is however witnessed by the diverse effects on the final composites.

According to our SAXS analysis (Table 2), the mineral component encompasses small NPs, not observed by AFM and the shape of which is difficult to univocally define by SAXS together with significantly larger platelets (imaged by AFM), likely originating from aggregation of the smaller ones, as suggested by the decrease of their volume fraction upon maturation. To the best of our knowledge, ACP of such platy morphology has never been reported in previous reports on collagen mineralization experiments, and is

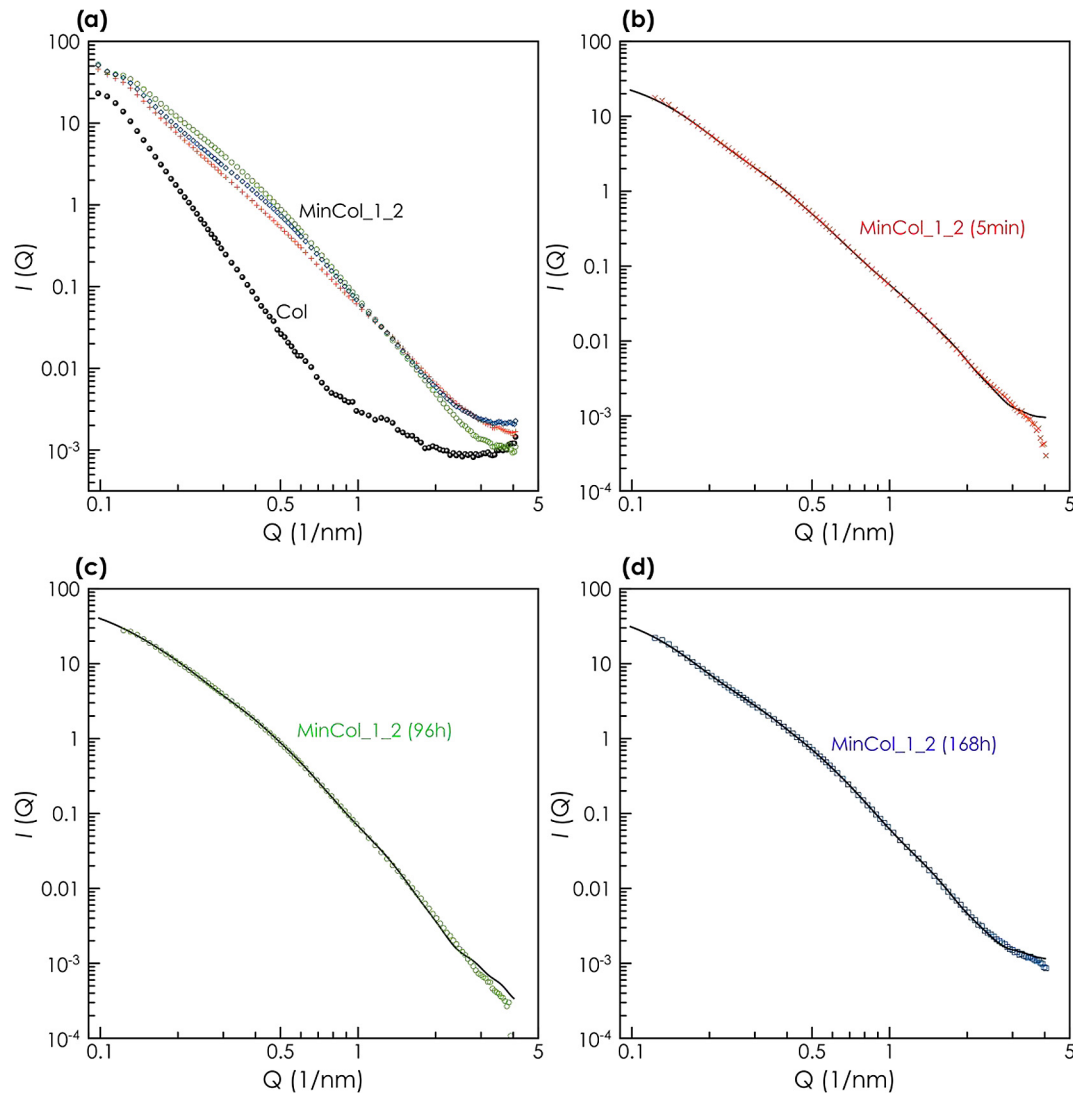


Fig. 4. a) SAXS patterns of non-mineralized (Col) and mineralized samples (MinCol_1_2), the latter at increasing maturation time (cross: 5 min; circles: 96 h; squares: 168 h). b-d) Best fits for the MinCol_1_2 samples using the combination of a tri-axial and ellipsoidal particles models. Here data are subtracted of the capillary and collagen scattering signals.

Table 2

Radii (in nm) of the bimodal distribution of spheres, ellipsoids of revolution and triaxial ellipsoids, as extracted from the fittings to the SAXS data. Standard deviations are given in brackets.

Aging time	Bimodal spheres		Ellipsoid of revolution		Tri-axial ellipsoid			η_1/η_2^2
	Radius 1	Radius 2	Radius	Height	a-axis	b-axis	c-axis	
5 min	2.3 (0.1)	1.3 (0.1)	4.0 (0.1)	1.2 (0.1)	25.3 (1.0)	16.5 (0.3)	4.4 (0.1)	0.57
96 h	2.8 (0.1)	1.6 (0.1)	3.7 (0.3)	1.6 (0.2)	30.3 (3.3)	15.2 (0.3)	4.0 (0.1)	0.24
168 h	1.9 (0.1)	1.4 (0.1)	3.1 (0.1)	1.4 (0.1)	27.2 (0.6)	18.4 (0.2)	3.4 (0.1)	0.24

a: η_1/η_2^2 is the relative volume fraction of ellipsoids of revolution (1) over triaxial ellipsoids (2). Similar values were obtained after considering the bimodal distribution of spheres as (1).

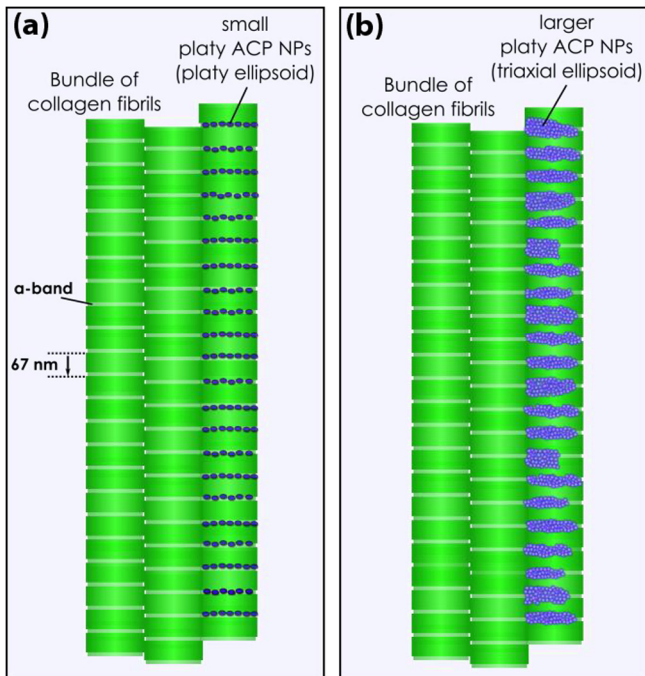


Fig. 5. Schematic view of the precipitation of platy ACP nanoparticles assisted by citrate and collagen. Citrate induces the formation of stable small NPs (with sizes ca. $4 \text{ nm} \times 1.2 \text{ nm}$) a). The larger ACP platelets likely originate from the aggregation of the smaller ones (b).

likely favoured by the templating role of collagen fibrils, on the surface of which the smallest NPs may start to aggregate. Very much as reported for negatively charged pAsp-ACP hybrids interacting with the positive N- and C-terminals of the collagen molecules, which promote their infiltration into the collagen fibrils [7], we interpret the “nearly periodic” arrangement of the ACP nanoplatelets imaged by AFM on the collagen fibril surface (Fig. 3d) by a similar structural/electrostatic effect. This suggests that citrate may play a role comparable to that of NCPs in mediating the mineral infiltration into collagen fibrils. Supporting this hypothesis, the ζ -potential of ACP prepared in the presence of citrate² was found to be $-10.4 \pm 3.5 \text{ mV}$, indicating that, analogously to pAsp, citrate induces the formation of negatively-charged amorphous NPs. As expected, electrostatic interactions pull them toward the positively charged groups of collagen fibrils protruding in the gap region (Fig. 5a), favouring, in our crude mechanistic description, the deposition of ACP nanoparticles exhibiting platy morphology (Fig. 5b). In order to obtain a deeper insight into the nature of the ACP-collagen interaction, we also performed FTIR analyses (Section S3 and Fig. S3, Supplementary data). However, these experiments did not provide any meaningful information, likely due to the small amount of ACP within the composites. Why the stability of ACP, in the conditions of the mineralization experiments here proposed, extends to several days (no transformation into a more stable crystalline phase being observed within one week) requires further studies. As a matter of fact, an increased stability of ACP, involving the formation of the so-called polymer-induced liquid-precursors (PILP), has been observed in the presence of organic molecules [1,18,45].

Our data also indicated that the intermolecular lateral packing is not affected by the precipitation of the amorphous precursors and remains constant upon maturation (Fig. 2a). This is consistent with the fact that the amorphous mineral is being deposited in the

nanosized holes of the gap regions (transversal to the bundles) but not in the (longitudinally spread) intermolecular collagen voids.

On the basis of these *in vitro* experiments and according to our previous reports on biomimetic citrated-covered apatites [24], we can postulate that citrate may both stabilize the amorphous precursor and provide it with negatively-charged surface, facilitating the electrostatic interaction with specific positively-charged groups of collagen fibrils. As a matter of fact, a similar control through the same mechanism has been proposed for NCPs. Notwithstanding, the much smaller size of citrate ions (than NCPs) brings about other consequences; beyond enabling the infiltration in the gap region, it is likely that sagittal permeation (*here, unobserved*) may be at work, although at a much slower pace.

5. Conclusions

Although citrate is an important component of bone organic matrix and has been found strongly bound on bone apatite nanocrystals, its specific role in bone mineral formation is unclear to date. In this manuscript, we have performed *in vitro* collagen mineralization experiments in the presence of citrate under physiological conditions (pH 7.4 and $37 \text{ }^\circ\text{C}$). We found that the mineral formation was completely inhibited by the *simultaneous* action of collagen and citrate (with a citrate/ Ca^{2+} ratio of 4), while, in the absence of one of the two organic components, nanoapatite is formed. However, using a lower citrate/ Ca^{2+} ratio, our WAXS experiments demonstrated the precipitation of ACP nanoparticles which *i)* are stable over time and *ii)* do not influence the lateral arrangement of collagen fibrils upon maturation, suggesting that the amorphous mineral does not infiltrate (longitudinally) within the fibrils. In addition, results from SAXS modeling and AFM observations confirmed the unusual platy morphology of the ACP, which are specifically deposited on the *a-band* of the collagen fibrils.

Whether the deposition of amorphous precursors with platy morphology is at work at the early stages of *in vivo* bone mineral formation, in the presence of a comparable environment (collagen, NCPs and citrate ions), cannot be derived from the present data. The similarity of the organic components and of the mineralizing solution *in vivo* and in our *in vitro* tests, however, paves the way for new studies, addressing some of the key factors responsible for the precipitation of markedly anisotropic nanoparticles within the intrafibrillar gap and considering the important role of citrate, traditionally neglected.

Acknowledgements

This work has been carried out in the framework of the project BioBone (Andalucía Talent Hub program: <http://www.juntadeandalucia.es/economiainnovacionyciencia/talentia/?q=node/12544>, co-funded by the Spanish Junta de Andalucía and EU-FP7 within the Marie Skłodowska-Curie Actions). Partial financial support was given to F.B. (University of Insubria Junior Grant, 2015). The authors thank Dr. Michele Iafisco (Institute of Science and Technology for Ceramics, ISTECCNR, Italy) for kindly providing the horse tendon type I collagen used in this work. The courtesy of Edison SpA for a long-term loaning of the AFM equipment to University of Insubria is also acknowledged. The authors thank the staff at the X04SA-MS Beamline of the SLS-PSI for technical support.

Appendix A. Supplementary data

Supplementary data associated with this article can be found, in the online version, at <http://dx.doi.org/10.1016/j.actbio.2016.11.041>.

² The PDF curve of this ACP is shown in Fig. 2b and the synthesis is described in detail in Ref. [24].

References

- [1] M.J. Olszta, X. Cheng, S.S. Jee, R. Kumar, Y.-Y. Kim, M.J. Kaufman, E.P. Douglas, L. B. Gower, Bone structure and formation: a new perspective, *Mater. Sci. Eng. R* 58 (2007) 77–116.
- [2] P. Fratzl, R. Weinkamer, Nature's hierarchical materials, *Prog. Mater. Sci.* 52 (2007) 1263–1334.
- [3] W. Landis, R. Jacquet, Association of calcium and phosphate ions with collagen in the mineralization of vertebrate tissues, *Calcif. Tissue Int.* 93 (2013) 329–337.
- [4] S. Weiner, H.D. Wagner, The material bone: structure-mechanical function relations, *Annu. Rev. Mater. Sci.* 28 (1998) 271–298.
- [5] M.J. Glimcher, H. Muir, Recent studies of the mineral phase in bone and its possible linkage to the organic matrix by protein-bound phosphate bonds [and discussion], *Philos. Trans. R. Soc. Lond. B Biol. Sci.* 304 (1984) 479–508.
- [6] J.Y. Rho, L. Kuhn-Spearing, P. Zioupos, Mechanical properties and the hierarchical structure of bone, *Med. Eng. Phys.* 20 (1998) 92–102.
- [7] F. Nudelman, K. Pieterse, A. George, P.H.H. Bomans, H. Friedrich, L.J. Brylka, P.A. J. Hilbers, G. de With, N. Sommerdijk, The role of collagen in bone apatite formation in the presence of hydroxyapatite nucleation inhibitors, *Nat. Mater.* 9 (2010) 1004–1009.
- [8] J.P.R.O. Orgel, T.C. Irving, A. Miller, T.J. Wess, Microfibrillar structure of type I collagen in situ, *Proc. Natl. Acad. Sci. U.S.A.* 103 (2006) 9001–9005.
- [9] L.C. Palmer, C.J. Newcomb, S.R. Kaltz, E.D. Spoerke, S.I. Stupp, Biomimetic systems for hydroxyapatite mineralization inspired by bone and enamel, *Chem. Rev.* 108 (2008) 4754–4783.
- [10] A. George, A. Veis, Phosphorylated proteins and control over apatite nucleation, crystal growth, and inhibition, *Chem. Rev.* 108 (2008) 4670–4693.
- [11] Y. Liu, N. Li, Y.-P. Qi, L. Dai, T.E. Bryan, J. Mao, D.H. Pashley, F.R. Tay, Intrafibrillar collagen mineralization produced by biomimetic hierarchical nanoapatite assembly, *Adv. Mater.* 23 (2011) 975–980.
- [12] Y. Wang, T. Azais, M. Robin, A. Vallée, C. Catania, P. Legriel, G. Pehau-Arnaudet, F. Babonneau, M.-M. Giraud-Guille, N. Nassif, The predominant role of collagen in the nucleation, growth, structure and orientation of bone apatite, *Nat. Mater.* 11 (2012) 724–733.
- [13] A.S. Deshpande, E. Beniash, Bioinspired synthesis of mineralized collagen fibrils, *Cryst. Growth Des.* 8 (2008) 3084–3090.
- [14] F. Nudelman, A.J. Lausch, N.A.J.M. Sommerdijk, E.D. Sone, In vitro models of collagen biomineralization, *J. Struct. Biol.* 183 (2013) 258–269.
- [15] J. Tao, K.C. Battle, H. Pan, E.A. Salter, Y.-C. Chien, A. Wierzbicki, J.J. De Yoreo, Energetic basis for the molecular-scale organization of bone, *Proc. Natl. Acad. Sci. U.S.A.* 112 (2015) 326–331.
- [16] F.H. Silver, W.J. Landis, Deposition of apatite in mineralizing vertebrate extracellular matrices: a model of possible nucleation sites on type I collagen, *Connect. Tissue Res.* 52 (2011) 242–254.
- [17] A.-W. Xu, Y. Ma, H. Colfen, Biomimetic mineralization, *J. Mater. Chem.* 17 (2007) 415–449.
- [18] L.B. Gower, Biomimetic model systems for investigating the amorphous precursor pathway and its role in biomineralization, *Chem. Rev.* 108 (2008) 4551–4627.
- [19] J. Mahamid, A. Sharif, L. Addadi, S. Weiner, Amorphous calcium phosphate is a major component of the forming fin bones of zebrafish: indications for an amorphous precursor phase, *Proc. Natl. Acad. Sci. U.S.A.* 105 (2008) 12748–12753.
- [20] J. Mahamid, B. Aichmayer, E. Shimon, R. Ziblat, C. Li, S. Siegel, O. Paris, P. Fratzl, S. Weiner, L. Addadi, Mapping amorphous calcium phosphate transformation into crystalline mineral from the cell to the bone in zebrafish fin rays, *Proc. Natl. Acad. Sci. U.S.A.* 107 (2010) 6316–6321.
- [21] R.L. Hartles, Citrate in mineralized tissues, *Adv. Oral Biol.* 1 (1964) 225–253.
- [22] Y.Y. Hu, A. Rawal, K. Schmidt-Rohr, Strongly bound citrate stabilizes the apatite nanocrystals in bone, *Proc. Natl. Acad. Sci. U.S.A.* 107 (2010) 22425–22429.
- [23] B. Xie, G.H. Nancollas, How to control the size and morphology of apatite nanocrystals in bone, *Proc. Natl. Acad. Sci. U.S.A.* 107 (2010) 22369–22370.
- [24] J.M. Delgado-López, R. Frison, A. Cervellino, J. Gómez-Morales, A. Guagliardi, N. Masciocchi, Crystal size, morphology, and growth mechanism in bio-inspired apatite nanocrystals, *Adv. Funct. Mater.* 24 (2014) 1090–1099.
- [25] A. Tampieri, G. Celotti, E. Landi, M. Sandri, N. Roveri, G. Falini, Biologically inspired synthesis of bone-like composite: self-assembled collagen fibers/hydroxyapatite nanocrystals, *J. Biomed. Mater. Res. A* 67A (2003) 618–625.
- [26] P.R. Willmott, D. Meister, S.J. Leake, M. Lange, A. Bergamaschi, M. Boge, M. Calvi, C. Cancellieri, N. Casati, A. Cervellino, Q. Chen, C. David, U. Flechsig, F. Gozzo, B. Henrich, S. Jaggi-Spielmann, B. Jakob, I. Kalichava, P. Karvinen, J. Krempasky, A. Ludeke, R. Luscher, S. Maag, C. Quitmann, M.L. Reinle-Schmitt, T. Schmidt, B. Schmitt, A. Streun, I. Vartiainen, M. Vitins, X. Wang, R. Wullschleger, The materials science beamline upgrade at the swiss light source, *J. Synchrotron Radiat.* 20 (2013) 667–682.
- [27] A. Cervellino, R. Frison, A. Guagliardi, in: N. Masciocchi, A. Guagliardi (Eds.), *Crystallography for Health and Biosciences*, Insubria Univ. Press, Varese, Italy, 2012, p. 177.
- [28] T. Egami, S.J.L. Billinge, *Underneath the Bragg Peaks: Structural Analysis of Complex Materials*, Elsevier, Amsterdam, 2012.
- [29] P. Juhas, T. Davis, C.L. Farrow, S.J.L. Billinge, PDFgetX3: a rapid and highly automatable program for processing powder diffraction data into total scattering pair distribution functions, *J. Appl. Crystallogr.* 46 (2013) 560–566.
- [30] A. Schwamberger, B. De Roo, D. Jacob, L. Dillemans, L. Bruegemann, J.W. Seo, J. P. Locquet, Combining SAXS and DLS for simultaneous measurements and time-resolved monitoring of nanoparticle synthesis, *Nucl. Instrum. Methods Phys. Res. Sect. B* 343 (2015) 116–122.
- [31] Y. Li, R. Beck, T. Huang, M.C. Choi, M. Divinagracia, Scatterless hybrid metal-single-crystal slit for small-angle X-ray scattering and high-resolution X-ray diffraction, *J. Appl. Crystallogr.* 41 (2008) 1134–1139.
- [32] J.S. Pedersen, Analysis of small-angle scattering data from colloids and polymer solutions: modeling and least-squares fitting, *Adv. Colloid Interface Sci.* 70 (1997) 171–210.
- [33] A.E.S. Van Driessche, J.M. García-Ruiz, J.M. Delgado-López, G. Sazaki, In situ observation of step dynamics on gypsum crystals, *Cryst. Growth Des.* 10 (2010) 3909–3916.
- [34] P. Fratzl, N. Fratzl-Zelman, K. Klaushofer, Collagen packing and mineralization. An x-ray scattering investigation of turkey leg tendon, *Biophys. J.* 64 (1993) 260–266.
- [35] E.D. Eanes, D.R. Lundy, G.N. Martin, X-ray diffraction study of the mineralization of turkey leg tendon, *Calcif. Tissue Res.* 6 (1970) 239–248.
- [36] G. Tronci, A. Doyle, S.J. Russell, D.J. Wood, Triple-helical collagen hydrogels via covalent aromatic functionalisation with 1,3-phenylenediacetic acid, *J. Mater. Chem. B* 1 (2013) 5478–5488.
- [37] C.L. Farrow, M. Shaw, H. Kim, P. Juhas, S.J.L. Billinge, Nyquist-Shannon sampling theorem applied to refinements of the atomic pair distribution function, *Phys. Rev. B* 84 (2011) 134105.
- [38] A.S. Posner, F. Betts, Synthetic amorphous calcium phosphate and its relation to bone mineral structure, *Acc. Chem. Res.* 8 (1975) 273–281.
- [39] A. Dey, P.H.H. Bomans, F.A. Müller, J. Will, P.M. Frederik, G. de With, N.A.J.M. Sommerdijk, The role of prenucleation clusters in surface-induced calcium phosphate crystallization, *Nat. Mater.* 9 (2010) 1010–1014.
- [40] K. Onuma, A. Ito, Cluster growth model for hydroxyapatite, *Chem. Mater.* 10 (1998) 3346–3351.
- [41] L. Wang, S. Li, E. Ruiz-Agudo, C.V. Putnis, A. Putnis, Posner's cluster revisited: direct imaging of nucleation and growth of nanoscale calcium phosphate clusters at the calcite-water interface, *CrystEngComm* 14 (2012) 6252–6256.
- [42] J. Christoffersen, M.R. Christoffersen, W. Kibalczyk, F.A. Andersen, A contribution to the understanding of the formation of calcium phosphates, *J. Cryst. Growth* 94 (1989) 767–777.
- [43] Y. Chen, W. Gu, H. Pan, S. Jiang, R. Tang, Stabilizing amorphous calcium phosphate phase by citrate adsorption, *CrystEngComm* 16 (2014) 1864–1867.
- [44] K. Chatzipanagis, M. Iafisco, T. Roncal-Herrero, M. Bilton, A. Tampieri, R. Kroger, J.M. Delgado-Lopez, Crystallization of citrate-stabilized amorphous calcium phosphate to nanocrystalline apatite: a surface-mediated transformation, *CrystEngComm* 18 (2016) 3170–3173.
- [45] S.S. Jee, T.T. Thula, L.B. Gower, Development of bone-like composites via the polymer-induced liquid-precursor (PILP) process. Part 1: influence of polymer molecular weight, *Acta Biomater.* 6 (2010) 3676–3686.